QUANTUM OPTICS

Entanglement distillation between solid-state quantum network nodes

N. Kalb,[1,2*] A. A. Reiserer,[1,2*†] P. C. Humphreys,[1,2*] J. J. W. Bakermans,[1,2] S. J. Kamerling,[1,2] N. H. Nickerson,[3] S. C. Benjamin,[4] D. J. Twitchen,[5] M. Markham,[5] R. Hanson[1,2‡]

The impact of future quantum networks hinges on high-quality quantum entanglement shared between network nodes. Unavoidable imperfections necessitate a means to improve remote entanglement by local quantum operations. We realize entanglement distillation on a quantum network primitive of distant electron-nuclear two-qubit nodes. The heralded generation of two copies of a remote entangled state is demonstrated through single-photon–mediated entangling of the electrons and robust storage in the nuclear spins. After applying local two-qubit gates, single-shot measurements herald the distillation of an entangled state with increased fidelity that is available for further use. The key combination of generating, storing, and processing entangled states should enable the exploration of multiparticle entanglement on an extended quantum network.

Future quantum networks connecting nodes of long-lived stationary qubits through photonic channels may enable secure communication, quantum computation and simulation, and enhanced metrology (*1–9*). The power of these applications fundamentally derives from quantum entanglement shared between the network nodes. The key experimental challenge is therefore to establish high-quality remote entanglement in the presence of unavoidable errors such as decoherence, photon loss, and imperfect quantum control. Notably, by only using classical communication and local quantum operations, a high-fidelity remote entangled state can be distilled from several lower-fidelity copies (*10*, *11*) (Fig. 1A). Success of this intrinsically probabilistic distillation can be nondestructively heralded by measurement outcomes such that the distilled state is available for further use, a critical requirement for scalable networks. Owing to these unique features, entanglement distillation (or purification) has become a central building block of quantum network proposals (*6–9*, *12*, *13*).

Generation and distillation of remote entangled states

To run entanglement distillation on a quantum network, several copies of a raw entangled state must first be shared between the nodes. This can be achieved by using a network primitive of two nodes with two qubits each: a communication qubit with an optical interface for generating remote entanglement and a memory qubit for storage (Fig. 1B). First, the communication qubits run the entangling protocol, which, owing to photon loss, is intrinsically probabilistic. After photon detection heralds the generation of a raw entangled state on the communication qubits, this state is swapped onto the memory qubits. The communication qubits are then used to generate a second raw entangled state. At this point, the network nodes share two nominally identical copies of the raw state, from which an entangled state of higher fidelity can be distilled. This protocol thus exploits the combination of heralded generation of remote entanglement with robust quantum state storage, high-fidelity quantum logic gates, and nondemolition qubit readout within each node.

These demanding experimental requirements have so far limited the exploration of distillation of entangled qubits to four ions within a single node (*14*) and to all-photonic protocols without memories in which the distilled state was unavoidably lost upon success (*15–17*). As an important step toward the desired quantum network, heralded entanglement between distant stationary qubits has recently been achieved with ions, atoms, nitrogen-vacancy (NV) defect centers, quantum dots, and superconducting qubits (*18–23*). However, the potential memory qubits investigated so far in conjunction with these protocols (*24*, *25*) suffered from rapid dephasing during remote entangling attempts because of unwanted couplings, thus precluding the generation of multiple remote entangled states as required for distillation.

We realize the distillation of entangled states on an elementary quantum network consisting of a pair of two-qubit solid-state nodes separated by 2 m (Fig. 1B). We implement a single-photon–based entangling protocol using diamond electron-spin qubits (communication qubits) while capitalizing on recent progress on quantum control (*26*) and robust state storage (*27*) in nuclear-spin–based quantum memories. Real-time feedback is implemented to compensate memory qubit phase shifts induced by the probabilistic nature of the remote entangling protocol. As an immediate advantage, the demonstrated protocol distinctly increases the efficiency of entanglement generation compared to the standard two-photon–coincidence protocols used in earlier works (*25*, *28*), while removing the optical path-length dependence of standalone probabilistic single-photon protocols (*22*, *29*).

Quantum network nodes

Our quantum network nodes comprise an NV electron spin in diamond as a communication qubit and a nearby carbon-13 nuclear spin as a memory qubit. The diamond chips holding these qubits reside in individual closed-cycle cryostats ($T = 4\,\mathrm{K}$) that are separated by 2 m (*30*). The electron spin state is manipulated by means of amplitude-shaped microwave pulses. Electron spin decoherence occurs on time scales exceeding a millisecond and has negligible impact on the presented results. Spin-selective resonant optical excitation enables high-fidelity initialization and single-shot nondemolition readout of the electron spin (*31*), as well as generation of spin-photon entanglement for connecting distant nodes (*20*) (see also fig. S4). We use nuclear spins with intrinsic dephasing times T_2^* of 3.4(1) ms and 16.2(3) ms for node A and B, respectively (*30*). We implement universal control on each of these nuclear spin qubits by exploiting its hyperfine coupling to the electron spin through recently developed dynamical-decoupling–based gate sequences (*32*). This complete quantum toolbox enables the implementation of all four steps in the distillation protocol.

Figure 1C shows the compilation of the full gate circuit into the quantum control operations of our platform. This compilation maximizes the repetition rate and minimizes the number of local quantum gates after the generation of the first remote state. In particular, by initializing the memory qubit at the start of the protocol, we can implement the SWAP operation with just two conditional quantum gates instead of the three that would be required for arbitrary input states (*30*). Note that our SWAP implementation maps the communication qubit energy eigenstates onto memory superposition states $|\pm X\rangle \equiv (|0\rangle \pm |1\rangle)/2$.

To benchmark the performance of the local quantum logic, we execute a combination of the SWAP (orange box in Fig. 1C) and the gates of the distillation step (purple box in Fig. 1C) to generate a maximally entangled Bell state between the communication and memory qubits (see Fig. 2A). The full density matrix of the resulting two-qubit state is reconstructed via quantum state tomography [QST; see (*30*) for further details]. We find a fidelity with the ideal Bell state of 0.96(1) [0.98(1)] for node A [B],

[1]QuTech, Delft University of Technology, Post Office Box 5046, 2600 GA Delft, Netherlands. [2]Kavli Institute of Nanoscience, Delft University of Technology, Post Office Box 5046, 2600 GA Delft, Netherlands. [3]Department of Physics, Imperial College London, Prince Consort Road, London SW7 2AZ, UK. [4]Department of Materials, University of Oxford, Parks Road, Oxford OX1 3PH, UK. [5]Element Six Innovation, Fermi Avenue, Harwell Oxford, Didcot, Oxfordshire OX11 0QE, UK.
*These authors contributed equally to this work.
†Present address: Quantum Networks Group, Max-Planck-Institute of Quantum Optics, Hans-Kopfermann-Strasse 1, 85748 Garching, Germany.
‡Corresponding author. Email: r.hanson@tudelft.nl

indicating high-quality operations in both nodes (Fig. 2B).

Robust storage of quantum information

A critical capability for the network nodes is the robust storage of quantum information in the memories while the communication qubits are used to generate remote entangled states. This requires the memory qubits to have long coherence times and be resilient to operations on the communication qubit. The generation of remote entanglement, in particular, poses two challenges as its probabilistic nature means that an a priori unknown number of attempts is required.

First, each failed entangling attempt leaves the communication qubits in an unknown state, which necessitates a reset by optical pumping. This reset is a stochastic process which, in combination with the always-on hyperfine interaction between communication and memory qubit, causes dephasing of stored memory states (*27*, *33*). Memories with a small parallel hyperfine coupling are used so that the precession frequency of these memories exhibits only a weak dependency $\Delta\omega$ on the state of the communication qubit during the repumping process of a few hundred nanoseconds [$\Delta\omega_A = 2\pi\cdot 22.4(1)$ kHz and $\Delta\omega_B = 2\pi\cdot 26.6(1)$ kHz]. Decoherence via the perpendicular hyperfine component is suppressed by an applied magnetic field of about 40 mT.

Second, the interaction between communication and memory qubits leads to a deterministic phase shift $\varphi_{A/B}$ on the memory per entangling attempt. Because it is unknown which entangling attempt will herald success, real-time feedback on the memory is required to compensate for these phase shifts before the final two-qubit gate of Fig. 1C is applied. In addition, the feedback must preserve the coherence of the communication qubit as it holds the second copy of the raw entangled state. We realize such real-time feedback through dynamical decoupling of the electron spin synchronized with the nuclear spin precession frequency that induces an electron-state–independent phase gate on the memory (*32*). At each node, the number of entangling attempts until success N is tracked by a microprocessor that terminates the subsequent decoupling sequence when the desired rotation $R_z(\varphi_{A/B})^N$ has been applied. Ideally, this leaves the memory with the desired phase relation regardless of the number of entangling attempts. We calibrate and verify this feedback at each node separately (Fig. 3, A and B) and measure a negligible effect on the memory state fidelity while the state of the communication qubit is preserved as desired.

With this feedback realized, we investigate the robustness of the memory as a function of the elapsed entangling attempts. The memory is initialized in one of the six cardinal states of the Bloch sphere ($|0\rangle, |1\rangle, |\pm X\rangle$, and $|\pm Y\rangle \equiv (|0\rangle \pm i|1\rangle)/\sqrt{2}$); a number of entangling attempts are then executed, followed by phase feedback and measurement of the relevant memory expectation value (Fig. 3C). Dephasing-sensitive states $|\pm X\rangle, |\pm Y\rangle$ decay with $1/e$ values of 273(5) [272(4)] entangling attempts in node A (node B), whereas the energy eigenstates $|0\rangle, |1\rangle$ are preserved with high fidelity, as expected. The memories thus provide faithful storage during remote entangling attempts.

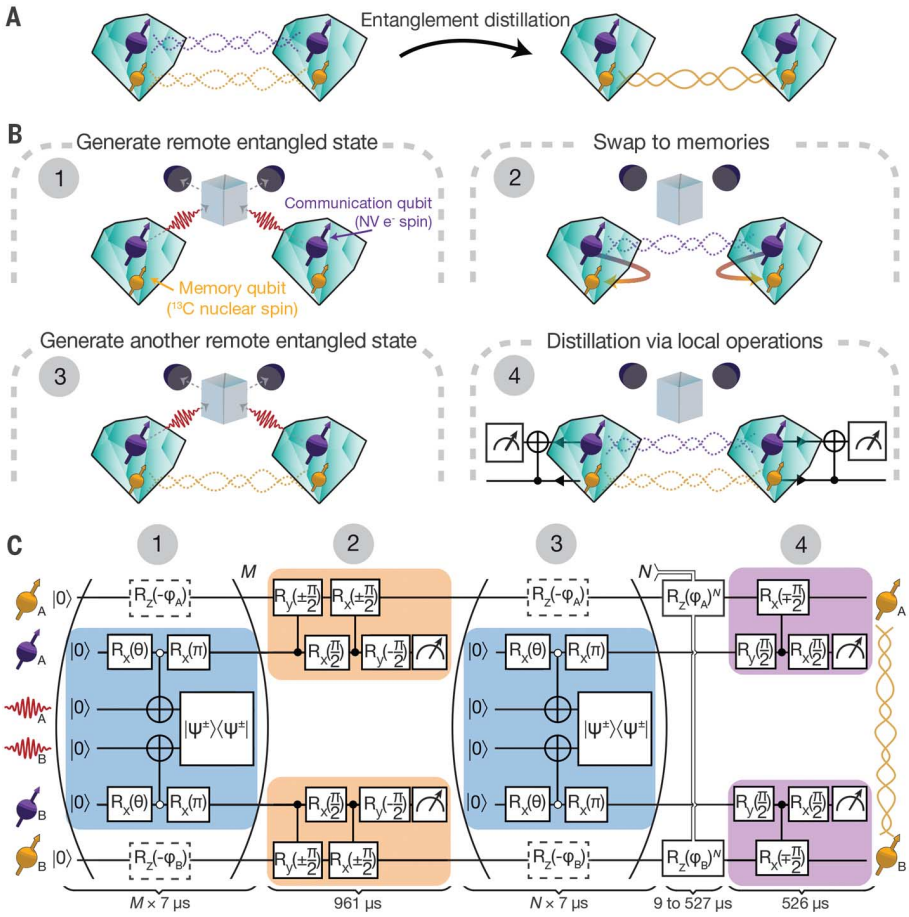

Fig. 1. Entanglement distillation on a quantum network. (**A**) Working principle: A remote entangled state of higher quality (right) is distilled via local operations and classical communication from several lower-quality states (left) that are shared between remote qubits (depicted as colored spins). (**B**) Protocol overview. Each network node consists of a communication qubit (purple) and a memory qubit (yellow). First, the communication qubits are prepared in a remote entangled state by generating entanglement between a photon (red wave packet) and the spin, interfering the optical modes on a beam splitter (gray cube) and subsequently detecting a single photon (1). Next, the remote entangled state (purple waves represent entanglement) is swapped onto the memory qubits (2), followed by another round of entangled state generation (3). Finally, local operations (black circuit) distill a state of higher fidelity (4). (**C**) Gate circuit implementing steps 1 to 4. We include the photonic modes of each setup (red wave packets) in which a qubit is encoded such that vacuum and a single photon represent $|0\rangle$ and $|1\rangle$, respectively. Entanglement between the electron spin and photonic mode is experimentally realized by an optical π-pulse (depicted as CNOT symbol). The photonic Bell-state projection $|\Psi^\pm\rangle\langle\Psi^\pm|$ is probabilistically realized by a beam splitter and subsequent detection of a single photon. Dashed-bordered gates indicate phase shifts of the memory due to free evolution during entangling attempts. Colored boxes indicate logical blocks of the circuit and are used throughout the manuscript.

Experimental entanglement distillation

With local control and storage in place, we now turn toward the execution of the full distillation protocol (figs. S1 and S2). Following Campbell's protocol (*34*), we generate the remote states that provide the resources for distillation by first initializing both communication qubits in a superposition with variable angle θ, $|\theta\rangle \equiv \sin\theta|0\rangle - i\cos\theta|0\rangle$. Subsequent optical excitation for state $|0\rangle$ and overlap of the emission of both communication qubits on a beam splitter (see steps 1 and 3 of Fig. 1C and histograms in fig. S3) generate the raw remote state ρ_{raw} if a single photon is detected (*34*). For equal and small detection probabilities for both nodes and negligible dark counts, ρ_{raw} reads

$$\rho_{raw} = (1-\sin^2\theta)|\Psi^\pm_\phi\rangle\langle\Psi^\pm_\phi| + \sin^2\theta|0,0\rangle\langle 0,0| \quad (1)$$

The states $|\Psi^\pm_\phi\rangle \equiv (|01\rangle \pm e^{i\phi}|10\rangle)/\sqrt{2}$ are entangled states, with a relative phase depending on which detector clicked ($\pm$) and an additional

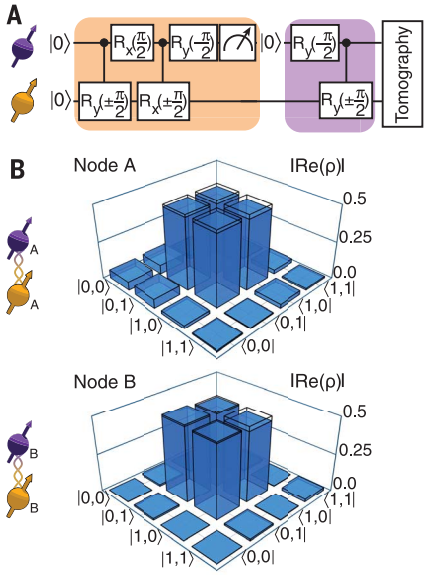

Fig. 2. Benchmarking local control. (**A**) Gate circuit for entanglement generation within one node. All local operations of the distillation circuit are used to generate an entangled state between communication and memory qubit. Color coding of local operations corresponds to Fig. 1C. (**B**) Absolute value of the real part of the local density matrix obtained via sequential QST [see fig. S9 and (*30*)]. We find fidelities with the desired entangled state of 0.96(1) (node A) and 0.98(1) (node B). Transparent bars give the values of the ideal state.

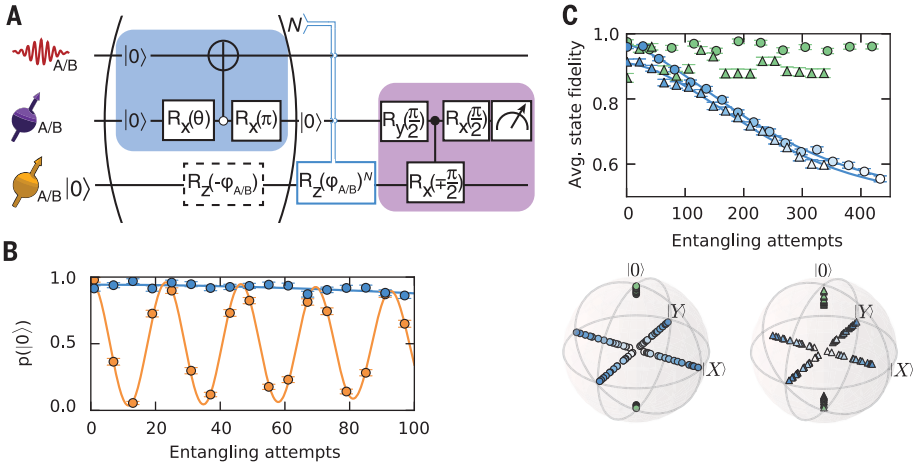

Fig. 3. Quantum state storage during entangling operations. (**A**) Real-time feedback circuit for memory qubits. We initialize memory A/B, which then experiences a phase shift of $-\varphi_{A/B}$ per executed entangling attempt. After reinitialization of the communication qubit, the distillation step of the protocol is performed (Fig. 1C). Blue-rimmed gate indicates the feedback. (**B**) Memory state as a function of the number of entangling attempts. The oscillation observed without feedback (orange) is successfully compensated (blue) by the feedback. Solid lines are fits to the data. (**C**) Memory lifetime of node A (triangles) and node B (circles). We initialize the memory in one of the six cardinal states of the Bloch sphere (see bottom panel), sweep the number of entangling attempts, apply feedback, and read out the expectation value that is relevant for the estimation of the state fidelity with the initial cardinal state. All fidelity-irrelevant expectation values are set to zero, i.e., we depict projections of the state onto the respective axis in the Bloch sphere picture. The average state fidelities are separately plotted for phase-sensitive superposition states (blue) and phase-insensitive eigenstates (green). Blue solid lines depict a generalized exponential fit (*30*). The decay is limited by the stochastic repumping process, microwave pulse errors, and/or environmental dephasing. The color gradient of the top and bottom panels matches to facilitate comparisons. Error bars represent one standard deviation (SD).

internal phase ϕ due to the unknown path length between both emitters and the beam splitter. The fraction of the nonentangled admixture $|0,0\rangle\langle 0,0|$ can be directly controlled through the choice of the initial communication qubit state $|\theta\rangle$; note that the choice of $|\theta\rangle$ also affects the probability of successful entanglement generation (scaling as $\sin^2\theta$). We next swap the raw state onto the memories such that the communication qubit is free for another round of remote state generation (step 2 in Fig. 1C). Once a second state is successfully generated (step 3), we apply a conditional quantum gate within each node and read out the communication qubits in a single shot. Owing to the quantum nondemolition nature of this readout, the memory qubits do not experience additional dephasing during this step (*31*). Readout of the communication qubit projects the memories into one of four states depending on the readout results (*30*):

$$(0_A, 0_B) : \frac{1}{2}\cos^4\theta U|\Psi_0^\pm\rangle\langle\Psi_0^\pm|U^\dagger$$

$$(0_A, 1_B) : \frac{1}{2}\sin^2\theta\cos^2\theta U(|0,1\rangle\langle 0,1| + |1,1\rangle\langle 1,1|)U^\dagger$$

$$(1_A, 0_B) : \frac{1}{2}\sin^2\theta\cos^2\theta U(|1,0\rangle\langle 1,0| + |1,1\rangle\langle 1,1|)U^\dagger$$

$$(1_A, 1_B) : \sin^4\theta U|1,1\rangle\langle 1,1|U^\dagger + \frac{1}{2}\cos^4\theta U|\Psi_{2\phi}^\pm\rangle\langle\Psi_{2\phi}^\pm|U^\dagger$$

Here the states are left unnormalized; their traces indicate their probabilities of occurrence. The unitary U corresponds to a Hadamard gate on each memory that arises from the swapping operation in each node. Observation of the readout combination $(0_A,0_B)$ heralds successful distillation and leaves the system in the state

$$|\psi\rangle_c \otimes |\psi\rangle_m = e^{i\phi}|0,0\rangle \otimes U|\Psi_0^\pm\rangle \qquad (2)$$

with the relative phase of the final Bell state given by the photon detection signature, i.e., the photons in steps 1 and 3 were detected in the same (+) or in different (–) output ports. Notably, the protocol is agnostic to correlated dephasing of the raw states and is therefore only sensitive to optical path-length drifts that occur within an individual run of the protocol (see fig. S7) (*34*). This is in stark contrast to probabilistic single-photon protocols (*22*, *23*, *29*, *35*) that require path-length stabilization over the full course of data acquisition.

The experimental implementation of entanglement generation requires that the communication qubits' optical transitions are kept on resonance despite shot-to-shot fluctuations and long-term drifts of the respective local charge environments. An automatic feedback loop and resonance search routine is used to compensate for charge jumps such that the experiment is push-button and runs without human intervention. To further optimize the data rate, the number of remote entangling attempts is bounded to 1000 for step 1 and up to 500 rounds for step 3, leading to event rates (i.e., two remote states were successfully generated) of around 10 Hz. These bounds are a compromise between maximizing the success probability (favoring more attempts) and minimizing effects of drifts and of memory decoherence (favoring fewer attempts).

Distillation results

We start by running the complete protocol using $\theta = \pi/6$ and perform full quantum state tomography on the distilled state. This way, using the complete information obtained on the resulting output, we can verify whether the protocol works as desired. Figure 4A shows the resulting data for a maximum of 50 entangling attempts in the second round of state generation. This truncation yields optimal state storage during each run of the protocol (*30*). Quantitatively, the measured fidelity with the ideal Bell state of 0.65(3) > 0.5 proves entanglement of the distilled state. Furthermore, the density matrix has high populations in the Bell-state subspace only, showing that the distillation successfully diminishes the separable admixture.

To gain further insight into the performance of the protocol, we measure the fidelity of the distilled state for different amounts of the separable admixture in the raw states; i.e., for different θ (see Fig. 4B, blue dots). The results are again truncated after a maximum of 50 entangling attempts in the

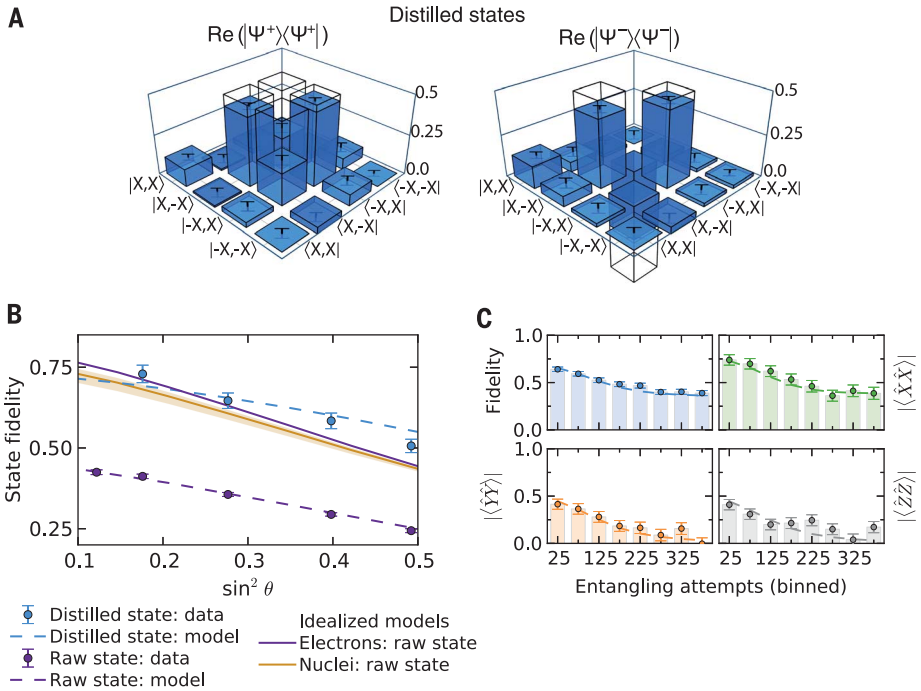

Fig. 4. Experimental realization of entanglement distillation. (**A**) Two-qubit density matrices for $\theta = \pi/6$ and a maximum of 50 entangling attempts in the second round. (Right) Different detectors clicked. (Left) The same detector clicked twice. We find a fidelity with the ideal state of 0.65(3) for both states. Transparent bars represent the ideal state. (**B**) Fidelity with the ideal state as a function of θ for a maximum of 50 entangling attempts in the second round. Blue data are the two-memory state fidelity. Dashed lines are derived from our model (*30*). Purple data are the measured raw state fidelity on the communication qubits. Solid orange (purple) line is the modeled fidelity of the raw state on the memories (communication qubits) that would be obtained if the initial internal phase was known. The memory state is calculated for the average number of entangling attempts until success (25). The orange shaded region is the modeled memory fidelity for minimal (0 attempts) and maximal (50 attempts) dephasing. The θ-dependence of the distilled state fidelity is explained by the finite probability of misidentifying a separable state (the presence of which scales with θ) as a successfully distilled entangled state owing to imperfect quantum control and decoherence of the stored state. Fidelities were obtained by measuring the expectation values $\langle\hat{X}\hat{X}\rangle$, $\langle\hat{Y}\hat{Y}\rangle$, and $\langle\hat{Z}\hat{Z}\rangle$. We denote the Pauli operators as $\hat{X}$, $\hat{Y}$, and $\hat{Z}$. (**C**) State decay for $\theta = \pi/6$. Data are binned according to the number of second entanglement generation attempts until success. Shown are the state fidelity (blue) and the absolute value of the relevant expectation values. The dashed lines are derived from our theoretical model (see fig. S5). Error bars represent 1 SD.

second round. The state fidelities are averaged over both detection signatures.

The hallmark of successful distillation is an increase in fidelity of the distilled state compared to that of the raw states. Whereas in the textbook description both raw states are assumed to be equal, in our experiment they are different owing to imperfections in the swap operation and memory storage that only affect the raw state held by the memories, and path-length variations on short time scales that only affect the raw state held by the communication qubits. To make a meaningful comparison, we therefore consider the state fidelities of each of these raw states separately.

Because of the unreferenced internal phase of the raw states, all coherences are washed out owing to optical path-length variations. Direct tomography will therefore yield state fidelities that cannot surpass 0.5. As a result, the measured fidelities of the distilled states far exceed the electron state fidelities measured after step 1 (Fig. 4B, purple dots). Although these numbers reflect the current experiment, we now turn to a more strict comparison by taking into account that the internal phase may become accessible in future experiments through optical path stabilization.

We model the raw state fidelities at the start of the distillation step (step 4) using independently determined parameters under the assumption of a perfectly known initial path-length difference (Fig. 4B, solid purple line for raw state on the electrons and solid orange line for raw state on the nuclei) (*30*). For small values of θ (small separable admixtures), the fidelity increase due to distillation is offset by the errors introduced with the additional quantum operations of the distillation step. However, we find that for larger values of θ, the distilled state fidelity significantly surpasses both of the raw state fidelities [see also fig. S10 and (*30*) for hypothesis test]. This result demonstrates the realization of entanglement distillation on our elementary quantum network.

For a more detailed understanding of the different error sources contributing to the measured fidelity, we develop an extensive model of the full protocol using independently measured quantities and two free parameters: one factor accounting for additional memory control errors and the second for phase fluctuations of the raw states (*30*). We find good agreement between the modeled fidelity and the data for each of the different separable admixtures [see Fig. 4B, blue dashed line, and (*30*)] and for the evolution of the correlations with the number of entangling attempts (Fig. 4C). The model indicates that the state fidelities are mainly limited by memory qubit dephasing and control errors, as well as nonzero two-photon distinguishability. The latter effect, quantified by a measured two-photon interference visibility of 0.73(3) (see fig. S6), is especially harmful in the above comparison with the raw state, as this occurs twice for the distillation protocol but only once for the raw state generation. A visibility of 0.9 as observed on different NV center pairs (*28*) would thus yield an even stronger entanglement enhancement.

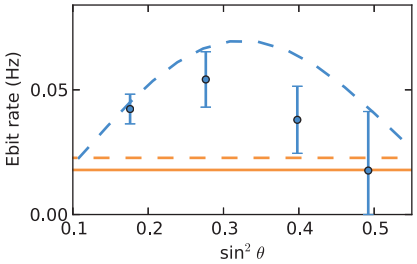

Fig. 5. Ebit rate comparison. Ebit rate as a function of excitation angle θ. The blue data are derived from the measured success rates and state fidelity over the entire data set (see fig. S8). The blue dashed line is the estimated ebit rate for distillation, including the overhead of local operations. The solid (dashed) orange line gives the estimated ebit rate of a standard two-photon protocol, including (excluding) imperfections. All data are averaged over both detection signatures. Error bars represent 1 SD.

Ebit rate

Previously demonstrated entangling protocols based on two-photon coincidences (*25*, *28*) require steps 1 and 3 to succeed in subsequent attempts, leading to a success probability scaling with the square of the photon detection probability p_{det}. By contrast, the distillation protocol allows step 3 to succeed in one of many attempts following success in step 1, leading to a

success probability scaling linearly with p_{det} in the ideal case. Given that in a typical quantum network setting p_{det} will be small (in our case, $p_{\mathrm{det}} \approx 10^{-3}$), the distillation protocol can provide a distinct rate advantage despite the overhead of the additional local quantum logic.

To quantitatively compare our results with two-photon–coincidence protocols, we set an upper bound on the rate r of entangled bit (ebit) generation for each protocol using $r = \nu E_{\mathrm{N}}$ with the logarithmic negativity E_{N} and the rate of success ν. Figure 5 compares the ebit rate of the presented distillation protocol to the modeled rate of the Barrett-Kok two-photon–coincidence protocol (*36*) used in earlier experiments on NV centers (*20*, *28*). We find that the distillation protocol (blue dots) outperforms the two-photon–coincidence protocol for identical experimental conditions, not only when assuming the measured two-photon indistinguishability (orange solid line) but even for the case in which the two-photon–coincidence protocol would be able to access perfect two-photon indistinguishability (orange dashed line).

Conclusion and outlook

The combination of generating, storing, and processing remote entangled qubits as demonstrated in the current distillation experiment provides a universal primitive for realizing extended quantum networks. The distillation itself is a powerful method to counteract unavoidable decoherence as entanglement is distributed throughout the network. Also, the protocol enables a speedup of entanglement generation that can be harnessed in related platforms such as other solid-state defect centers (*37*) and trapped ions (*38*). Improvements can be expected by encoding qubits into decoherence-protected subspaces (*27*), by using isotopically purified materials with longer qubit dephasing times (*39*–*41*), by implementing a faster reset or a measurement-based reset of the communication qubit, and by increasing the entangling rates through photonic cavities (*42*, *43*). Furthermore, the techniques used in recent demonstrations of multi-qubit control and quantum error correction on a four-qubit node (*26*, *44*) are fully compatible with the current experiment, thus highlighting the potential for scaling to more qubits and extending network functionality in the near future. Finally, the methods developed provide the toolkit to explore and utilize many-particle entanglement on a multinode quantum network.

REFERENCES AND NOTES

1. H. J. Kimble, *Nature* **453**, 1023–1030 (2008).
2. M. Ben-Or, C. Crepeau, D. Gottesman, A. Hassidim, A. Smith, *47th Annual IEEE Symposium on Foundations of Computer Science* (2006).
3. A. Broadbent, J. Fitzsimons, E. Kashefi, *50th Annual IEEE Symposium on Foundations of Computer Science* (2009).
4. L. Jiang *et al.*, *Phys. Rev. A* **79**, 032325 (2009).
5. A. Ekert, R. Renner, *Nature* **507**, 443–447 (2014).
6. J. I. Cirac, A. K. Ekert, S. F. Huelga, C. Macchiavello, *Phys. Rev. A* **59**, 4249–4254 (1999).
7. D. Gottesman, T. Jennewein, S. Croke, *Phys. Rev. Lett.* **109**, 070503 (2012).
8. N. H. Nickerson, J. F. Fitzsimons, S. C. Benjamin, *Phys. Rev. X* **4**, 041041 (2014).
9. P. Kómár *et al.*, *Nat. Phys.* **10**, 582–587 (2014).
10. C. H. Bennett *et al.*, *Phys. Rev. Lett.* **76**, 722–725 (1996).
11. D. Deutsch *et al.*, *Phys. Rev. Lett.* **77**, 2818–2821 (1996).
12. W. Dür, H.-J. Briegel, J. I. Cirac, P. Zoller, *Phys. Rev. A* **59**, 169–181 (1999).
13. L. Childress, J. M. Taylor, A. S. Sørensen, M. D. Lukin, *Phys. Rev. Lett.* **96**, 070504 (2006).
14. R. Reichle *et al.*, *Nature* **443**, 838–841 (2006).
15. J.-W. Pan, S. Gasparoni, R. Ursin, G. Weihs, A. Zeilinger, *Nature* **423**, 417–422 (2003).
16. P. G. Kwiat, S. Barraza-Lopez, A. Stefanov, N. Gisin, *Nature* **409**, 1014–1017 (2001).
17. J.-W. Pan *et al.*, *Rev. Mod. Phys.* **84**, 777–838 (2012).
18. D. L. Moehring *et al.*, *Nature* **449**, 68–71 (2007).
19. J. Hofmann *et al.*, *Science* **337**, 72–75 (2012).
20. H. Bernien *et al.*, *Nature* **497**, 86–90 (2013).
21. A. Narla *et al.*, *Phys. Rev. X* **6**, 031036 (2016).
22. A. Delteil *et al.*, *Nat. Phys.* **12**, 218–223 (2016).
23. R. Stockill *et al.*, arXiv:1702.03422 [quant-ph] (2017).
24. W. Pfaff *et al.*, *Science* **345**, 532–535 (2014).
25. D. Hucul *et al.*, *Nat. Phys.* **11**, 37–42 (2015).
26. J. Cramer *et al.*, *Nat. Commun.* **7**, 11526 (2016).
27. A. Reiserer *et al.*, *Phys. Rev. X* **6**, 021040 (2016).
28. B. Hensen *et al.*, *Nature* **526**, 682–686 (2015).
29. L. Slodička *et al.*, *Phys. Rev. Lett.* **110**, 083603 (2013).
30. Materials and methods are available as supplementary materials.
31. M. S. Blok *et al.*, *Nat. Phys.* **10**, 189–193 (2014).
32. T. H. Taminiau, J. Cramer, T. van der Sar, V. V. Dobrovitski, R. Hanson, *Nat. Nanotechnol.* **9**, 171–176 (2014).
33. L. Jiang *et al.*, *Phys. Rev. Lett.* **100**, 073001 (2008).
34. E. T. Campbell, S. C. Benjamin, *Phys. Rev. Lett.* **101**, 130502 (2008).
35. C. Cabrillo, J. I. Cirac, P. García-Fernández, P. Zoller, *Phys. Rev. A* **59**, 1025–1033 (1999).
36. S. D. Barrett, P. Kok, *Phys. Rev. A* **71**, 060310 (2005).
37. D. J. Christle *et al.*, *Nat. Mater.* **14**, 160–163 (2015).
38. C. Monroe, J. Kim, *Science* **339**, 1164–1169 (2013).
39. G. Balasubramanian *et al.*, *Nat. Mater.* **8**, 383–387 (2009).
40. P. C. Maurer *et al.*, *Science* **336**, 1283–1286 (2012).
41. A. M. Tyryshkin *et al.*, *Nat. Mater.* **11**, 143–147 (2011).
42. A. Faraon, P. E. Barclay, C. Santori, K.-M. C. Fu, R. G. Beausoleil, *Nat. Photonics* **5**, 301–305 (2011).
43. A. Sipahigil *et al.*, *Science* **354**, 847–850 (2016).
44. N. Kalb *et al.*, *Nat. Commun.* **7**, 13111 (2016).

ACKNOWLEDGMENTS

We thank T. H. Taminiau, E. T. Campbell, D. DiVincenzo, M. Lukin, T. Northup, L. M. K. Vandersypen, and S. Wehner for fruitful discussions. We acknowledge support from the Engineering and Physical Sciences Research Council National Quantum Technology Hub in Networked Quantum Information Technology (S.C.B.), the Netherlands Organisation for Scientific Research (NWO) through a VICI grant (R.H.), and the European Research Council through a Starting Grant (R.H.). Data contained in this paper are archived at https://doi.org/10.4121/uuid:9ccff914-1a8c-4d64-9ac3-b06122b86c5e.

SUPPLEMENTARY MATERIALS

www.sciencemag.org/content/356/6341/928/suppl/DC1
Materials and Methods
Tables S1 to S4
Figs. S1 to S10
References (*45*–*48*)

2 March 2017; accepted 9 May 2017
10.1126/science.aan0070

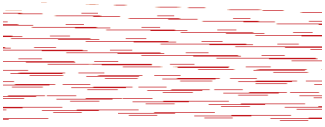

Entanglement distillation between solid-state quantum network nodes

N. Kalb, A. A. Reiserer, P. C. Humphreys, J. J. W. Bakermans, S. J. Kamerling, N. H. Nickerson, S. C. Benjamin, D. J. Twitchen, M. Markham and R. Hanson (June 1, 2017)

Science **356** (6341), 928-932. [doi: 10.1126/science.aan0070]

Editor's Summary

Entangle, swap, purify, repeat

The key to a successful quantum internet will be the ability to generate robust entanglement between distant quantum memories. Unavoidable interactions with the environment, however, generally result in the loss of entanglement. Kalb *et al.* describe an entanglement distillation protocol that could be used to enhance the purity and robustness of entanglement between quantum nodes of a primitive quantum network.

Science, this issue p. 928